Journal of Materials Chemistry A

ROYAL SOCIETY OF CHEMISTRY

PAPER

View Article Online
View Journal | View Issue

Cite this: J. Mater. Chem. A, 2024, 12, 9574

3D bridge-arch-structured dual-side evaporator for practical, all-weather water harvesting and desalination†

Meijie Chen, *[a] Shuang Li,[a] Xingyu Chen,[a] Yimou Huang,[a] Bin Liu,[a] Hongjie Yan,[a] Brian W. Sheldon, [b] Qing Li *[a] and Changmin Shi *[b]

Received 5th February 2024
Accepted 7th March 2024

DOI: 10.1039/d4ta00875h

rsc.li/materials-a

Environmentally friendly solar-driven evaporation shows great potential for desalination. However, conventional solar-driven evaporation in high-salinity brine results in low water purification efficiency due to salt accumulation on the evaporator surface. Additionally, the total water yield performance is further reduced in the absence of sunlight, significantly limiting its practical applications. To overcome these challenges, we proposed a highly efficient 3D bridge-arch-structured dual-side evaporator composed of Cu/CuO-polypyrrole for all-weather water harvesting and desalination *via* solar thermal and Joule heating. Our design results in an indoor evaporation rate of 4.10 kg m^{-2} h^{-1} during the daytime under one sun and 6.50 kg m^{-2} h^{-1} *via* Joule heating with a small voltage of 1.9 V during the nighttime. In addition, the designed evaporator results in a high evaporation rate of 3.60 kg m^{-2} h^{-1} in a water reservoir containing 10 wt% brine. At a practical level, the designed 3D evaporator achieved a high outdoor water yield rate of 10.69 kg m^{-2} day^{-1}. This performance represents a major step towards the commercialization of all-weather water harvesting and desalination.

Introduction

The lack of fresh water is a critical challenge in the quest to build a sustainable world, particularly in regions predominantly covered by desert.[1,2] To overcome this global challenge, seawater desalination,[3–6] wastewater purification,[7] and atmospheric water harvesting,[8–12] have been proposed as environmentally friendly approaches to collect fresh water. Among them, solar-driven seawater desalination emerges as a highly promising approach to generate fresh water, due to the abundance of solar energy and the high efficiency of the desalination process during the daytime when the sunlight intensity is high enough.[13–15]

Over past decades, various interfacial solar-driven evaporator structures, including nanoparticle dispersions,[16,17] 2D planes,[18–23] and 3D architectures[24–27] have been developed to improve evaporation performance. These innovations focus on improving solar thermal conversion,[28–30] regulating water supply,[31–33] reducing latent heat,[34–37] minimizing heat loss,[38–41] latent heat recovery,[42–45] and reducing salt-accumulation on the evaporators[46–50] in long-term desalination. However, the state-of-the-art solar-driven evaporators are time-dependent, with their efficiency fluctuating daily due to changes in sunlight intensity.[51,52] This results in a limited operational timeframe, significantly impacting their performance in all weather conditions.[45,46] In addition, high salt accumulation, particularly from high-salinity seawater (>3.5%), on the evaporators significantly reduces solar absorption, leading to less efficient fresh water generation. Therefore, the development of a highly efficient, all-weather evaporator capable of stable performance under high-salinity conditions is urgent.

Inspired by the capillary phenomenon of porous structures in nature and the arch bridge structure in architecture, we introduced a novel and highly efficient 3D bridge-arch-structured dual-side evaporator for all-weather desalination *via* solar-thermal heating in the daytime and Joule heating in the nighttime. The solar absorptance of the Cu foam was limited, and can be greatly improved by establishing black CuO blade nanoplates,[7] but the evaporation enthalpy is too high and limits the evaporation rate. Polypyrrole (PPy) can be sprayed on the surface of the Cu/CuO foam to form Cu/CuO-PPy foam to further reduce the evaporation enthalpy.[53] The combination of CuO and PPy both increased the solar absorptance and reduced the evaporation enthalpy, which greatly improved the evaporation rate. The Cu/CuO-PPy foam was bent into a 3D bridge-arch structure, and dual-side evaporation can be achieved and thermal conduction loss to the bulk water body can be reduced.

Our design achieved an exceptionally high solar absorptance of 0.944, due to the synergistic absorption effects of CuO and

[a]School of Energy Science and Engineering, Central South University, Changsha 410083, China. E-mail: chenmeijie@csu.edu.cn; qingli@csu.edu.cn

[b]School of Engineering, Brown University, Providence 02912, Rhode Island, USA. E-mail: changmin_shi@brown.edu

† Electronic supplementary information (ESI) available. See DOI: https://doi.org/10.1039/d4ta00875h

polypyrrole (PPy) on the Cu foam substrate. With our unique architecture, a continuous high evaporation rate with high-salinity brine can be achieved and salt accumulation can be easily dissolved into the water reservoir. During the daytime, the indoor solar-driven water evaporation was up to 4.10 kg m^{-2} h^{-1} under one sun. In the nighttime, the water evaporation rate *via* Joule heating was up to 6.50 kg m^{-2} h^{-1} at a voltage of 1.9 V. At a practical level, our designed 3D bridge-arch evaporator showed a high-water evaporation rate of ~3.60 kg m^{-2} h^{-1} in 10 wt% brine for 8 hours under one sun. In addition, the all-weather water yield was up to 10.69 kg m^{-2} day^{-1}. These achievements are a major step towards the commercialization of all-weather desalination evaporators for fresh water collection.

Results and discussion

Property characterization of the 3D dual-side evaporator

The fabrication schematic and working principle of our design are shown in Fig. 1A and B, respectively. To achieve all-weather evaporation *via* solar thermal and Joule heating, the evaporator should be electrically conductive and have high solar absorptance. Therefore, copper foam was selected as the framework material, owing to its flexibility and robustness, which also enables it to be easily folded into a 3D structure. To enhance solar absorption and water supply capabilities, the original Cu foam underwent a modification process. Initially, it was chemically etched to form CuO on the Cu foam. This was followed by *in situ* polymerization to apply a coating of PPy on the Cu/CuO foam. Completing this process, a dual-side 3D evaporator was created by folding the Cu/CuO-PPy foam into the desired shape. Detailed fabrication processes can be found in the Experimental section.

The chemically etched Cu foam significantly enhanced light absorption, attributable to the bandgap reduction and the generated needle-like CuO surface chemistry (Fig. 1C–E). By *in situ* polymerization, the black PPy particles can be attached to the Cu/CuO foam (Fig. 1F). The high content of N and S elements around the Cu/CuO-PPy foam also confirmed the formation of *in situ* polymerized PPy particles (Fig. S1†). Without the needle-like CuO, the Cu-PPy foam exhibited a relatively smooth skeleton (Fig. S2†) with a limited solar absorptance of ~0.874. In contrast, the solar absorptance of the Cu/CuO-PPy foam reached a maximum of ~0.944, surpassing that of Cu/CuO (~0.894) and Cu (~0.372) (Fig. 1G). Consequently, the evaporation enthalpy of water in the Cu/CuO-PPy foam was reduced to 1245 J g^{-1}, significantly lower than that of the water reservoir (2443 J g^{-1}). This reduction is attributed to the foam's multi-level micro-structure and the presence of intermediate water which has a low hydrogen bonding energy from the PPy, as shown in Fig. 1H and S3.†

The wetting ability of the water/evaporator interface and the supply of water against gravity are crucial factors in the evaporation process. With our design, the contact angle (CA) was 0° in the dried Cu/CuO, Cu-PPy, and Cu/CuO-PPy foams, in which water droplets would rapidly spread out at 34 ms. However, the non-treated Cu foam exhibited a strong hydrophobicity with a contact angle (CA) of 124° even after 60 s (Fig. S4†). Concerning water supply capability in the evaporator, the wicking velocity of the Cu/CuO-PPy was 0.042 m s^{-1} with a saturated waterfront level of 37 mm (Fig. 1I), while it was 0.033 m s^{-1} for Cu/CuO with a saturated waterfront level of 23 mm (Fig. S5†). Lacking sub-micro needle-like CuO, the Cu-PPy foam failed to generate sufficient capillary force (as shown in Fig. S2†) to supply water against gravity, similar to the issue with the original Cu foam (Fig. S6†).

The solar-thermal conversion performance over a wide incident angle was also investigated to illustrate the feasibility of our design. Given the achieved multi-level microstructure of the Cu/CuO-PPy foam, the temperature only dropped by 16.1 °C from a vertical incident angle of 0° to 60.1 °C under a simulated solar intensity of one sun, when the oblique incident angle was 75° (Fig. 1J). This demonstrated high suitability in the practical scenarios with sunrise and sunset.

Indoor daytime evaporation performance evaluation *via* solar thermal heating

To understand the mechanism of evaporation enhancement through the solar thermal heating process, we evaluated the indoor solar-driven evaporation performance using different architectural evaporators under simulated solar intensity (Fig. 2A). The evaporation rate was 4.10 kg m^{-2} h^{-1} by a dual-side 3D evaporator (Fig. 2B) under one sun. Based on the energy balance,[54–57] the evaporation efficiency was calculated to be 86.6% (Note S1†).

For a single-side evaporator and 2D evaporator, the evaporation rates were only 2.91 kg m^{-2} h^{-1} and 2.44 kg m^{-2} h^{-1}, respectively, under 1 sun (Fig. 2B). Spraying PPy onto the Cu/CuO foam significantly enhanced the solar evaporation rate, increasing it from 2.00 to 2.44 kg m^{-2} h^{-1} for the 2D evaporator (as shown in Fig. S7†) under one sun. This improvement is attributed to the increased evaporation area, enhanced solar absorption, increased water supply, and reduction in evaporation enthalpy brought about by the PPy coating.

Furthermore, the energy-mass transfer behavior was investigated to optimize the overall evaporation performance. When the width of the 3D dual-side evaporator was fixed at 1.5 cm (Fig. 2C), the evaporation rate peaked at a folding angle of 45° with 4.10 kg m^{-2} h^{-1} under one sun (Fig. 2D). When the folding angle was fixed at 45° (Fig. 2E), the evaporation rate peaked at the evaporator height of 1.8 cm with 4.10 kg m^{-2} h^{-1} under one sun (Fig. 2F). These results indicated that the taller 3D dual-side evaporator would result in a lower water supply rate (Fig. 1I), while a shorter counterpart led to a smaller evaporation area (Fig. 2B). Therefore, energy-mass transfer processes should be balanced to boost the evaporation performance. As a tradeoff, the dual-side 3D evaporator with the geometric parameters of a folding angle of 45°, height of 1.8 cm, and width of 1.5 cm was selected for further performance evaluation.

Based on the optimized parameters, the designed dual-side 3D evaporator showed excellent solar-driven evaporation performance under different solar intensities (Fig. 2G). The

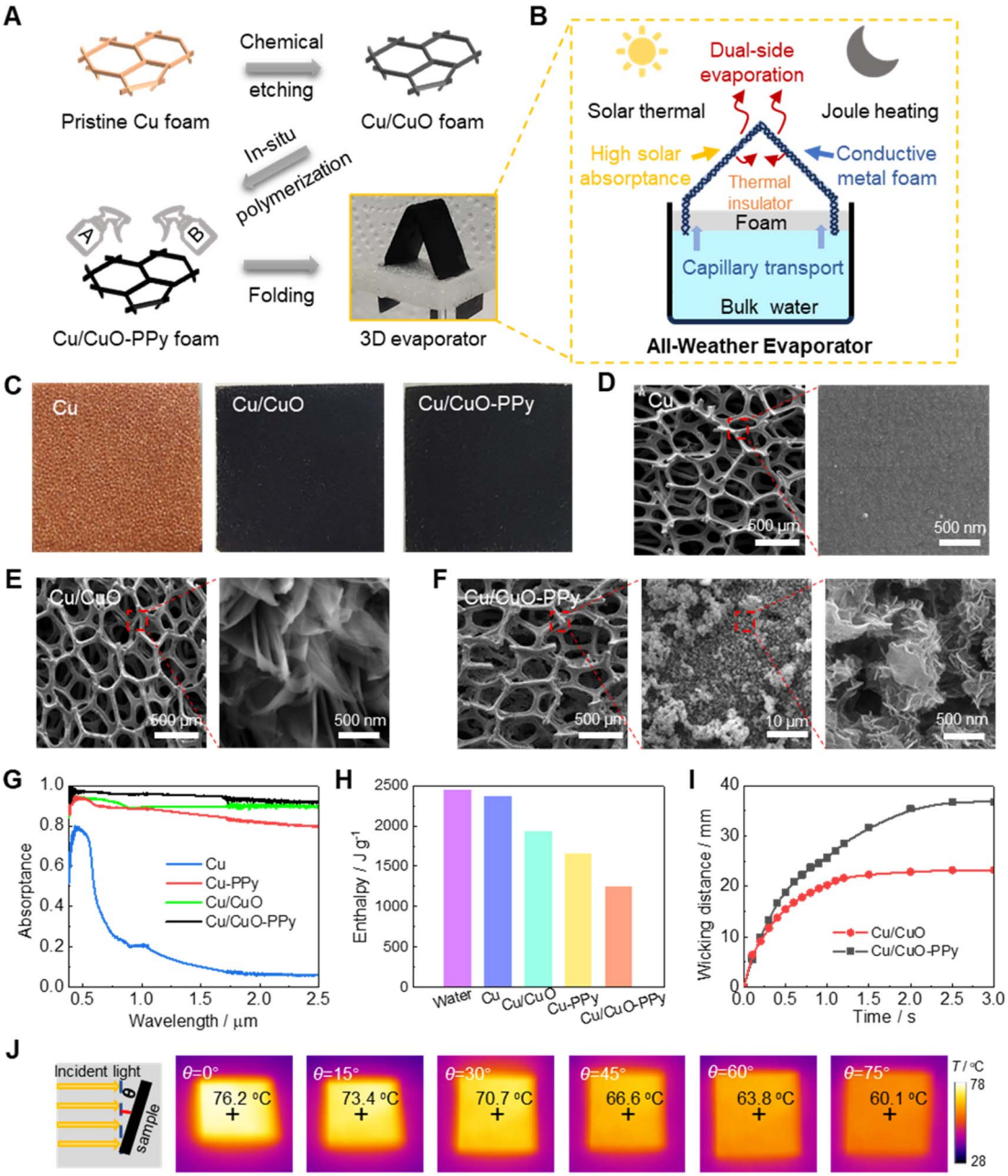

Fig. 1 Characterization of the 3D evaporator. (A) Fabrication process schematic of the 3D evaporator; (B) energy and mass transfer schematic diagram of the all-weather evaporator with solar thermal heating in the daytime and Joule heating in the nighttime; (C) optical photographs (width: 2 cm) of the evaporator with different compositions; (D)–(F) scanning electron microscopy (SEM) images of the evaporator with different compositions: (D) the original Cu foam, (E) Cu/CuO foam, and (F) Cu/CuO-PPy foam; (G) absorption spectra of the evaporator with different compositions; (H) measured evaporation enthalpy of pure water and water in Cu foam, Cu-PPy foam, Cu/CuO foam, and Cu/CuO-PPy foam; (I) time-dependent waterfront levels of Cu/CuO and Cu/CuO-PPy foam based on capillary water transport property measurements; (J) temperature distribution of the Cu/CuO-PPy foam evaporator at various incident angles (0°, 15°, 30°, 45°, 60°, and 75°) under one sun.

evaporation rate was 2.55 kg m^{-2} h^{-1} under half sun and 5.68 kg m^{-2} h^{-1} under two suns (Fig. 2H). Our designed evaporator showed excellent evaporation performance, which is far beyond the state-of-art designed materials (Fig. 2I and Table S1†), for example, plasmonic materials,[58–60] semiconducting materials,[52,61,62] carbon materials and conjugated polymers,[63–65] and hybrid photothermal materials.[66–68]

Indoor nighttime evaporation performance *via* Joule heating

Due to our unique electrically conductive designed Cu/CuO-PPy evaporator, it can be heated by Joule-heating using a DC power supply (Fig. 3A). This led to an efficient evaporation potential under dark conditions. The electric resistance of the Cu/CuO-PPy foam was only ~0.175 Ω (Fig. 3B). The dried Cu/CuO-PPy foam achieved steady temperatures of 37.2 °C, 58.1 °C, 72.2 °

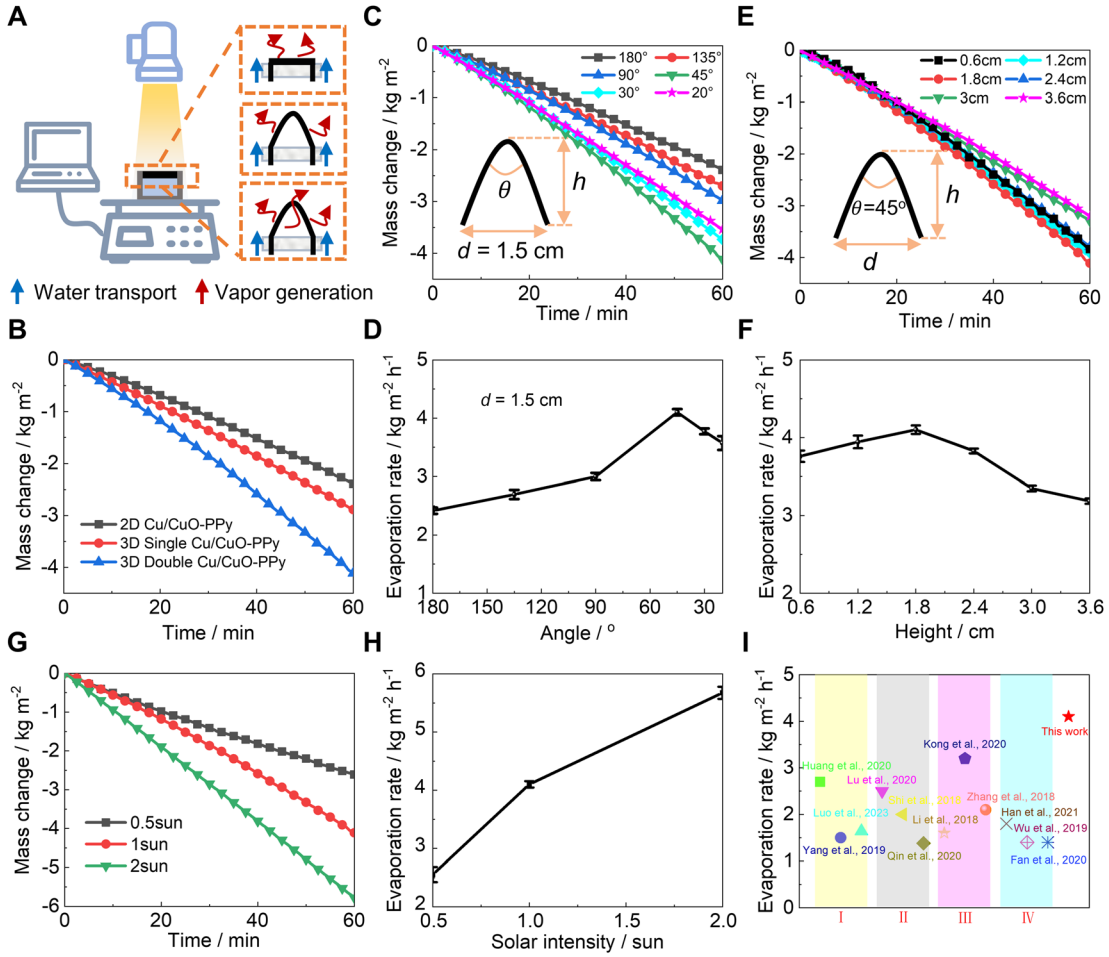

Fig. 2 Evaporation performance *via* solar thermal heating. (A) Schematic diagram of the setup for the water evaporation performance test with dual-side 3D, single-side 3D, and 2D planar evaporators; (B) mass change curves of dual-side 3D, single-side 3D, and 2D planar evaporators based on the Cu/CuO-PPy foam under one sun; (C) mass change curves and (D) evaporation rates of dual-side 3D evaporators at different folding angles under one sun; (E) mass change curves and (F) evaporation rates of dual-side 3D evaporators at different heights under one sun; (G) mass change curves and (H) evaporation rates of dual-side 3D evaporators under half sun, one sun, and two sun; (I) evaporation rates of the designed 3D evaporator compared with published data: (I) plasmonic materials,[58–60] (II) semiconductor materials,[52,61,62] (III) carbon materials and conjugated polymers,[63–65] and (IV) hybrid solar-thermal materials.[66–68]

C, and 97.0 °C (size: 20 mm × 20 mm × 1 mm) at 0.4 V, 0.9 V, 1.3 V, and 1.8 V, respectively (Fig. 3C). The results indicated that the Cu/CuO-PPy foam can be used for Joule heating with relatively low voltages. In addition, current–voltage (*CV*) curves of the Cu/CuO-PPy foam in dried and wet states were also measured (Fig. 3D). The resistance in the wet state (~0.162 Ω) was slightly smaller than that in the dried state (~0.175 Ω). The evaporation rates of the designed dual-side 3D evaporator induced by Joule heating were 1.59 kg m^{-2} h^{-1} (0.5 V), 2.73 kg m^{-2} h^{-1} (0.9 V), 4.16 kg m^{-2} h^{-1} (1.4 V), and 6.50 kg m^{-2} h^{-1} (1.9 V), as shown in Fig. 3E and F. Due to the poor water transport capacity of the Cu foam and Cu-PPy foam, evaporation experiments for these materials weren't conducted. Since the Cu/CuO foam exhibited lower electrical conductivity and a higher evaporation enthalpy than Cu/CuO-PPy, its evaporation rate was lower than that of the Cu/CuO-PPy foam (Fig. S8†). Local Joule heating inside the evaporator can be observed, which results in heating of the evaporator without increasing the temperature of the water reservoir. The evaporation temperature at the surface layer of the 3D dual-side evaporator, facing the outdoor environment, increased from 26.3 °C at 0.5 V to 36.4 °C at 1.9 V, as shown in Fig. 3G.

Salt-accumulation evaluation

To evaluate the salt accumulation of the 3D dual-side evaporator, indoor solar-driven evaporation with different brines was conducted (Fig. 4A). The water evaporation rates were 4.10 kg m^{-2} h^{-1}, 3.73 kg m^{-2} h^{-1}, 3.60 kg m^{-2} h^{-1}, and 3.53 kg m^{-2} h^{-1} with brine concentrations of 0 wt%, 3.5 wt%, 10 wt%, and 26.5 wt%, respectively. This showed that the designed evaporator can maintain a high evaporation rate in high salinity water. The long-term daytime stability of the evaporation was also analyzed. Upon continuously evaporating 10 wt% brine water for 8 hours (Fig. 4B), the evaporation rate was between 3.51 and 3.65 kg m^{-2} h^{-1}. In addition, the spectral absorptance of the Cu/CuO-PPy foam changed little before and after soaking in seawater for 12 h (Fig. S9†).

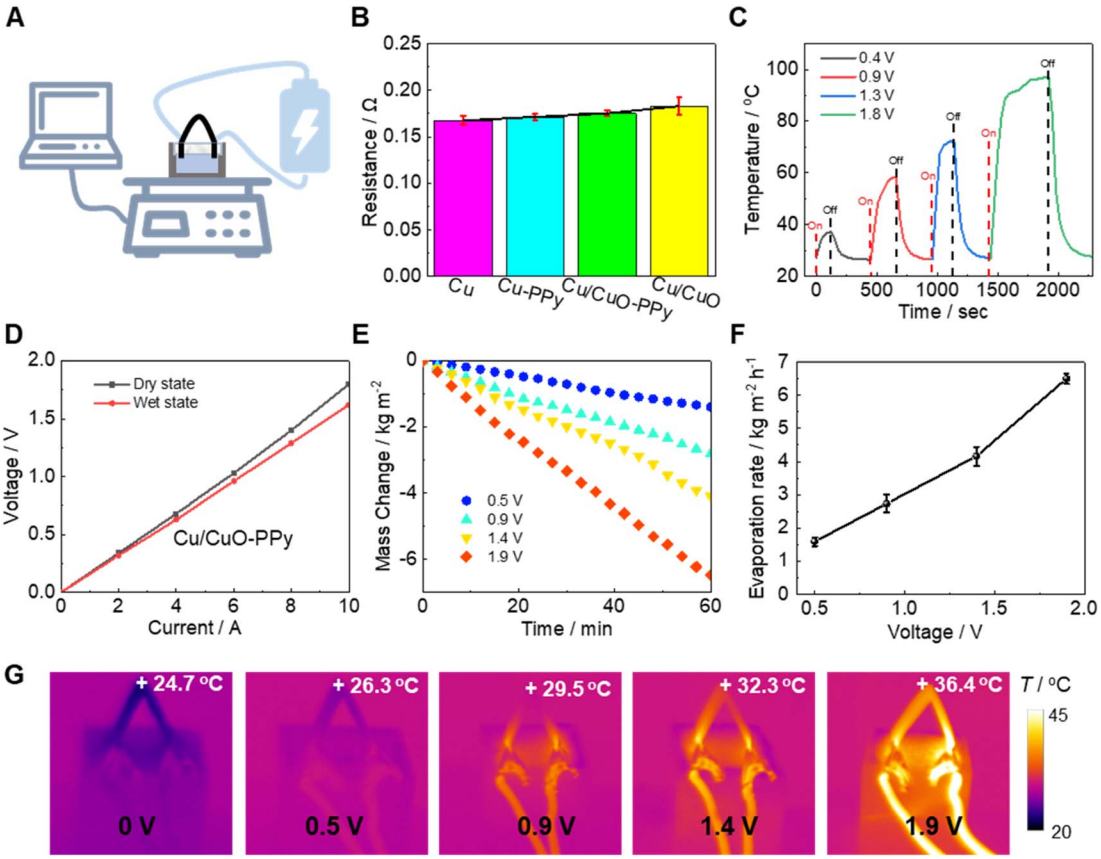

Fig. 3 Night time evaporation performance *via* Joule heating. (A) Schematic illustration of the evaporation driven by Joule heating; (B) electrical resistance of dried Cu, Cu/CuO, Cu-PPy, and Cu/CuO-PPy foams; (C) temperature changes of dried Cu/CuO–PPy foam (20 mm × 20 mm × 1 mm) subjected to different voltages; (D) *CV* curves of the Cu/CuO-PPy foam under dried and wet conditions; (E) mass changes and (F) evaporation rates of the dual-side 3D evaporator driven by Joule-heating at different voltages; (G) steady-state temperature of the dual-side 3D Cu/CuO–PPy evaporator subjected to different voltages.

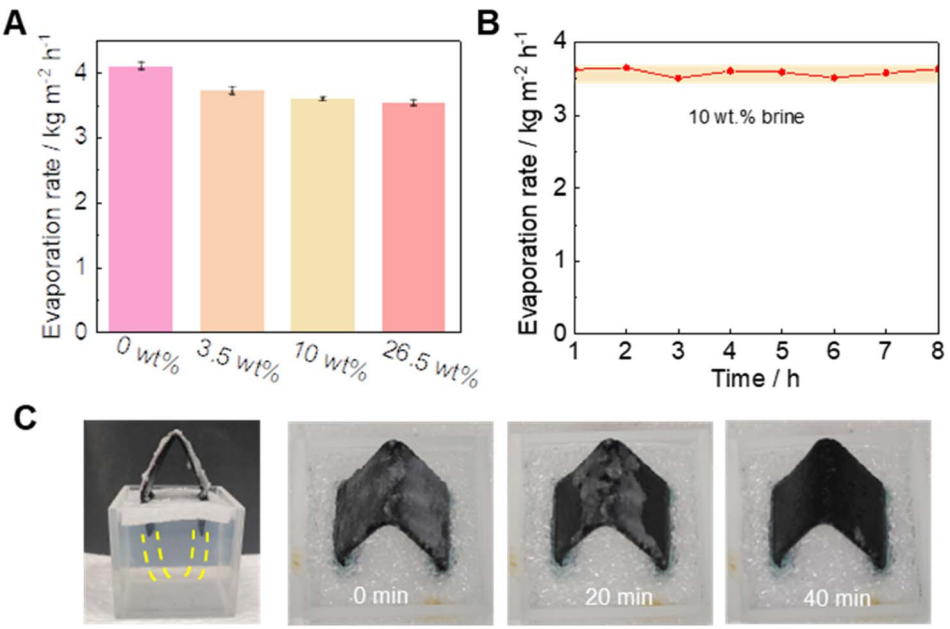

Fig. 4 Salt accumulation evaluation. (A) Daytime evaporation performance of the dual-side 3D evaporator in 3.5, 10, and 26.5 wt% brines; (B) evaporation rates of the 3D evaporator in 10 wt% brine for 8 hours under one sun; (C) salt accumulation evaluation of the 3D dual-side evaporator due to the quick salt ion diffusion process.

In addition, the crystallized salt on the surface of the evaporator can be easily dissolved in the water reservoir due to the high ion transport performance in the porous 3D structure (Fig. 4C). For example, 2.5 g NaCl crystal can immediately redissolve and return to the water reservoir (10 wt% brine) in 40 min at nighttime. This result indicated that even if salt accumulation occurred after long-term water evaporation, the salt could diffuse back into the water reservoir, which effectively avoided salt accumulation.

Outdoor water yield performance of the 3D dual-side evaporator

The all-weather outdoor evaporation performance evaluation setup is shown in Fig. S10.† The experiment was conducted in the daytime with an average solar intensity of 798.5 W m^{-2} and relative humidity of 40.4% (Fig. 5A). The surface layer of the 3D dual-side evaporator, facing the outdoor environment, maintained a temperature similar to ambient (42.5 °C *versus* 42.0 °C) due to evaporative cooling. Meanwhile, the water reservoir reached a higher temperature of 52.7 °C due to solar heating, as illustrated in Fig. 5B. This resulted in a higher evaporation rate of 4.95 kg m^{-2} h^{-1}, surpassing the indoor rate of 4.10 kg m^{-2} h^{-1} under an increased solar intensity of one sun, shown in Fig. 5C.

During the nighttime, the water evaporation *via* Joule heating was conducted at 1.7 V under an average relative humidity of 72.6% (Fig. 5D). The surface layer of the 3D dual-side evaporator facing the outdoor environment exhibited a maximum temperature (41.2 °C) due to the local Joule heating, while the water reservoir maintained a temperature of 34.4 °C (Fig. 5E). This led to an outdoor evaporation rate of 6.34 kg m^{-2} h^{-1} (Fig. 5F), which was a similar level to the indoor performance (6.50 kg m^{-2} h^{-1}) under Joule heating upon applying the same voltage. These results showed that the designed dual-side 3D evaporator achieved excellent evaporation performance in practical scenarios.

The outdoor water yield performance was evaluated based on the achieved evaporation performance (Fig. S11†). During the daytime *via* a solar thermal process, the water yield rate increased with solar intensity. At a peak solar intensity of

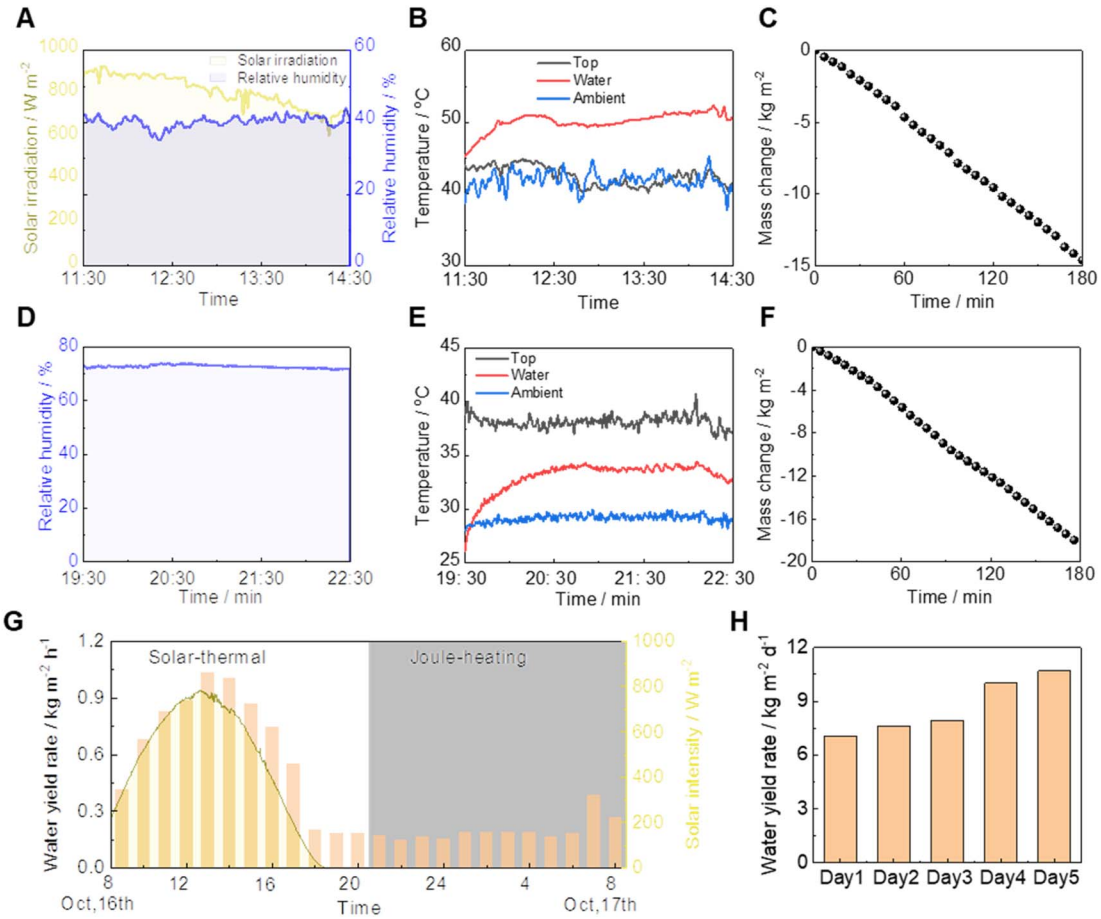

Fig. 5 Outdoor evaporation performance. (A) Meteorological parameters (solar intensity and relative humidity), and (B) temperature monitoring of the surface layer of the 3D dual-side evaporator facing the outdoor environment (labelled 'top'), water reservoir, and ambient environment at 11:30–14:30, 2023-07-11; (C) mass change of the dual-side evaporator in the outdoor experiment *via* solar thermal heating; (D) relative humidity, and (E) temperature monitoring of the surface layer of the 3D dual-side evaporator facing the outdoor environment (labelled 'top'), water reservoir, and ambient environment at 19:30–22:30, 2023-09-30; (F) mass change of the dual-side evaporator in the outdoor experiment *via* Joule heating (1.7 V). (G) All-weather water yield rate per hour during the daytime *via* solar thermal heating and nighttime *via* Joule heating (1.7 V). (H) Total water yield per day for five days of experiments.

approximately 760 W m^{-2}, the peak water yield rate reached 1.04 kg m^{-2} h^{-1}, resulting in an average daytime water yield rate of 0.72 kg m^{-2} h^{-1}. During the nighttime, the water yield rate stabilized at ~0.20 kg m^{-2} h^{-1} due to a constant Joule heating power (Fig. 5G). Furthermore, the daily water yield was assessed over five additional days, yielding results between 7.04 and 10.69 kg m^{-2} day^{-1} (Fig. 5H), influenced by different meteorological conditions (Fig. S12†). This resulted in an average harvest of around 10 kg of drinkable pure water per square meter outdoors, with the total energy consumption for Joule heating amounting to approximately 0.2 kW h, thereby incurring a negligible electricity cost. Notably, the water yield rate was substantially lower than the evaporation rate. This can be ascribed to the rate discrepancy between the evaporation and condensation sides.

Conclusion

In summary, we developed a highly efficient 3D biomimetic bridge-arch-structured dual-side evaporator for all-weather desalination *via* solar thermal and joule heating. The as-designed Cu/CuO-PPy foam demonstrated a high solar absorptance (~0.944), low evaporation enthalpy (1245 J g^{-1}), and high water supply rate (0.042 m s^{-1}). The 3D structure enabled dual-side evaporation with minimal thermal conductive loss to the water reservoir. By optimizing the geometric dimensions to balance the evaporation area and water supply, a high indoor evaporation rate of 4.10 kg m^{-2} h^{-1} was achieved under one sun. Additionally, the indoor evaporation rate through Joule heating (1.9 V) reached 6.50 kg m^{-2} h^{-1}. The Cu/CuO-PPy foam-based 3D evaporator also demonstrated an excellent evaporation rate of ~3.60 kg m^{-2} h^{-1} for 8 hours with a water reservoir containing 10 wt% brine. Outdoor experiments also showed that our designed 3D dual-side evaporator can achieve a high evaporation rate, with a maximum water yield rate reaching 10.69 kg m^{-2} day^{-1}. This demonstrates its potential as a solution for all-weather water harvesting using solar thermal and Joule heating.

Materials and methods

Fabrication of Cu/CuO-PPy foam

The Cu foam with a pore diameter of ~0.1 mm and a thickness of 1 mm was provided by YunZongCheng Technology (Jiangsu, China). Cu foam was immersed in a mixture of $NaClO_2$, NaOH, $Na_3PO_4 \cdot 12H_2O$, and DI water (3.75 : 5 : 10 : 100 wt%) at ~95 °C for 10 min. Polypyrrole (PPy) was polymerized and sprayed on the Cu/CuO foam. 2.74 g of $(NH_4)_2S_2O_8$ was dissolved in 5 mL of DI water, and was labeled as monomer A. Then, 0.84 mL of pyrrole was completely dissolved with 5 mL of isopropyl alcohol (IPA) and 1.84 mL of phytic acid (50 wt% water), and was labeled as monomer B. Next, monomers A and B were sprayed on Cu/CuO foam in the order B–A–B–A to obtain the designed Cu/CuO-PPy foam.

Characterization

SEM images were recorded by an MIRA3 LMH EDS: one Max 20 manufactured by TESCAN. The accelerated SEM voltage was 20.0 kV with magnifications of 100×, 500×, 5k×, and 100k×. Optical measurements were performed using a fiber optic spectrometer (0.3 μm–1.0 μm for PG2000, 1.0 μm–1.7 μm for NIR-1700) with an integrating sphere (IS-50-10-R). For the mid-infrared band (1.7 μm–2.5 μm), the spectra were measured by a Fourier transform infrared spectrometer (Nicolet iS50) with a gold integrating sphere and a wide-band MCT detector (Pike Technology). A high-speed camera was used to photograph the process of water dripping on the surface of the four samples, and then the contact angle was calculated using the high dosage method. The enthalpy of evaporation was measured by DSC 214. The wet sample was put into the crucible and measured at a linear heating rate of 10 K min^{-1} in the temperature range of 20 °C–160 °C, and the area integration of the heat flux curve and the horizontal coordinate time axis can be used to obtain the evaporation enthalpy of each sample. The Cu/CuO foam and Cu/CuO-PPy foam were cut into a long strip shape of 35 mm by 10 mm wide, and the upper end was fixed on an iron rack with a clip. A colorimetric dish filled with water was placed directly below, and a scale was placed behind it as a reference. The height was adjusted so that the lower end of the sample was in contact with the water surface. The liquid level rise heights of the foam were characterized using a camera. Finally, software called Nano Measure was used to measure the corresponding liquid level height at different times.

Indoor evaporation experiments

A solar xenon lamp (CEL-S500) was used to simulate sunlight, and a solar meter (TES-1333R) was used to measure the solar intensity. The ambient temperature during the indoor test was 24–26 °C and the relative humidity was 55–65%. The Cu foam was folded into different evaporators. Then, the evaporator was fixed on the insulation foam. The two sides of the evaporator penetrated the insulation foam and touched the water reservoir. The evaporator along with the insulation foam was floated in the square cavity, which was placed on the electronic balance (SQP, Sartorius) by adding an insulation foam between the cavity and the balance to reduce heat loss. The continuous mass change of the evaporation system was recorded with an electronic balance connected to a PC for real-time monitoring. The ambient temperature and relative humidity were recorded with a hygrometer (TRSi, TA622B). The real-time temperature change was recorded by K-type thermocouples connected with a data acquisition instrument (34970A, KEYSIGHT). Infrared images were recorded by an infrared thermal imager (i400, FLUKE). A DC power supply (HCP1024H, Henghui) was used to apply different currents at the two sides of the evaporator without sunlight.

Outdoor evaporation experiments

Outdoor evaporation experiments mirrored the indoor setup, with the key difference being the replacement of the solar simulator with natural sunlight. Outdoor experiments were conducted on a rooftop at Changsha, Hunan Province on July 11, 2023, for 3 h in the daytime and 3 h at night. The real-time solar irradiance was recorded by a solar radiometer, and the

ambient humidity was recorded by a hygrometer. The ambient temperature, the surface temperature of the evaporator, and the temperature of the water reservoir were recorded by K-type thermocouples. For water yield experiments, the evaporator with a 3D origami structure was put in a transparent acrylic container. The bottom of the device was sealed with polyethylene film to prevent steam from escaping. The water was collected actively per hour and weighed. The outdoor water collection experiments were carried out on a roof at Changsha, Hunan Province on September 17 to 19, October 15 to 16, and October 18, 2023.

Data availability

The data that support the findings of this study are available upon reasonable request from the authors.

Author contributions

M. C. and S. L. conceived and planned this research; S. L., Y. H., and X. C. did the experiments; M. C., S. L., X. C., Y. H., B. L., H. Y., Q. L., and C. S. performed data analysis; M. C. and S. L. wrote the manuscript. M. C., C. S. and Q. L. supervised this work. All authors contributed to the manuscript, discussed the results, and approved the final version of the manuscript.

Conflicts of interest

The authors declare no conflict of interest.

Acknowledgements

This work was financially supported by the National Key Research and Development Program of China (2022YFE0134400), the National Natural Science Foundation of China (52006246, 52176093), and the Central South University Innovation-Driven Research Programme (2023CXQD012).

Notes and references

1 M. M. Mekonnen and A. Y. Hoekstra, Four billion people facing severe water scarcity, *Sci. Adv.*, 2016, **2**, e1500323.
2 G. H. Cycles, W. W. Resources, S. Kanae and N. Series, Global Hydrological Cycles and World Water Resources, *Science*, 2015, **313**, 1068–1072.
3 P. Cao, L. Zhao, J. Zhang, L. Zhang, P. Yuan, Y. Zhang and Q. Li, Gradient Heating Effect Modulated by Hydrophobic/Hydrophilic Carbon Nanotube Network Structures for Ultrafast Solar Steam Generation, *ACS Appl. Mater. Interfaces*, 2021, **13**, 19109–19116.
4 Z. Wang, T. Horseman, A. P. Straub, N. Y. Yip, D. Li, M. Elimelech and S. Lin, Pathways and challenges for efficient solar-thermal desalination, *Sci. Adv.*, 2019, **5**, 1–12.
5 J. J. Koh, G. J. H. Lim, Y. Zhang, S. Liu and C. He, Robust, 3D-printed hydratable plastics for effective solar desalination, *Nano Energy*, 2020, **79**, 105436.
6 Y. Geng, K. Jiao, X. Liu, P. Ying, O. Odunmbaku, Y. Zhang, S. C. Tan and L. Li, Applications of bio-derived/bio-inspired materials in the field of interfacial solar steam generation, *Nano Res.*, 2022, **15**, 3122–3142.
7 N. Xu, J. Li, Y. Wang, C. Fang, X. Li, Y. Wang, L. Zhou and B. Zhu, A water lily – inspired hierarchical design for stable and efficient solar evaporation of high-salinity brine, *Sci. Adv.*, 2019, **5**, eaaw7013.
8 H. Shan, C. Li, Z. Chen, W. Ying, Z. Ye, Q. Pan, J. Wang and R. Wang, Exceptional water production yield enabled by batch-processed portable water harvester in semi-arid climate, *Nat. Commun.*, 2022, **13**, 5406.
9 Z. Yu, T. Zhu, J. Zhang, M. Ge, S. Fu and Y. Lai, Fog Harvesting Devices Inspired from Single to Multiple Creatures : Current Progress and Future Perspective, *Adv. Funct. Mater.*, 2022, **32**, 2200359.
10 Z. Xi, S. Li, L. Yu, H. Yan and M. Chen, All-Day Freshwater Harvesting by Selective Solar Absorption and Radiative Cooling, *ACS Appl. Mater. Interfaces*, 2022, **14**, 26255–26263.
11 W. Zhou, C. Zhou, C. Deng, L. Chen, X. Zeng, Y. Zhang, L. Tan, B. Hu, S. Guo, L. Dong and S. C. Tan, High-Performance Freshwater Harvesting System by Coupling Solar Desalination and Fog Collection with Hierarchical Porous Microneedle Arrays, *Adv. Funct. Mater.*, 2022, **32**, 2113264.
12 L. Yu, Y. Huang, W. Li, C. Shi, B. W. Sheldon, Z. Chen and M. Chen, Radiative-coupled evaporative cooling: Fundamentals, development, and applications, *Nano Research Energy*, 2023, **3**, e9120107.
13 P. Tao, G. Ni, C. Song, W. Shang, J. Wu, J. Zhu, G. Chen and T. Deng, Solar-driven interfacial evaporation, *Nat. Energy*, 2018, **3**, 1031–1041.
14 C. Chen, Y. Kuang and L. Hu, Challenges and Opportunities for Solar Evaporation, *Joule*, 2019, **3**, 683–718.
15 E. Jones, M. Qadir, M. T. H. Van Vliet, V. Smakhtin and S. Kang, The state of desalination and brine production : A global outlook, *Sci. Total Environ.*, 2019, **657**, 1343–1356.
16 O. Neumann, C. Feronti, A. D. Neumann, A. Dong, K. Schell, B. Lu and E. Kim, Compact solar autoclave based on steam generation using broadband light-harvesting nanoparticles, *Proc. Natl. Acad. Sci. U. S. A.*, 2013, **110**, 11677–11681.
17 Y. Liu, S. Yu, R. Feng, A. Bernard, Y. Liu and Y. Zhang, A Bioinspired , Reusable , Paper-Based System for High-Performance Large-Scale Evaporation, *Adv. Mater.*, 2015, **27**, 2768–2774.
18 H. Ren, M. Tang, B. Guan, K. Wang, J. Yang, F. Wang, M. Wang, J. Shan, Z. Chen, D. Wei, H. Peng and Z. Liu, Hierarchical Graphene Foam for Efficient Omnidirectional Solar – Thermal Energy Conversion, *Adv. Mater.*, 2017, **29**, 1702590.
19 Y. Xia, Q. Hou, H. Jubaer, Y. Li, Y. Kang, S. Yuan, H. Liu, M. W. Woo, L. Zhang, L. Gao, H. Wang and X. Zhang, Spatially isolating salt crystallisation from water evaporation for continuous solar steam generation and salt harvesting, *Energy Environ. Sci.*, 2019, **12**, 1840–1847.

20 X. Zhou, F. Zhao, Y. Guo, B. Rosenberger and G. Yu, Architecting highly hydratable polymer networks to tune the water state for solar water purification, *Sci. Adv.*, 2019, **5**, eaaw5484.

21 H. Yu, D. Wang, H. Jin, P. Wu, X. Wu, D. Chu, Y. Lu, X. Yang and H. Xu, 2D MoN1.2-rGO Stacked Heterostructures Enabled Water State Modification for Highly Efficient Interfacial Solar Evaporation, *Adv. Funct. Mater.*, 2023, **33**, 2214828.

22 Y. Lu, H. Zhang, Y. Wang, X. Zhu, W. Xiao, H. Xu, G. Li, Y. Li, D. Fan, H. Zeng, Z. Chen and X. Yang, Solar-Driven Interfacial Evaporation Accelerated Electrocatalytic Water Splitting on 2D Perovskite Oxide/MXene Heterostructure, *Adv. Funct. Mater.*, 2023, **33**, 2215061.

23 B. Shao, Y. Wang, X. Wu, Y. Lu, X. Yang, G. Y. Chen, G. Owens and H. Xu, Stackable nickel–cobalt@polydopamine nanosheet based photothermal sponges for highly efficient solar steam generation, *J. Mater. Chem. A*, 2020, **8**, 11665–11673.

24 W. Xu, X. Hu, S. Zhuang, Y. Wang, X. Li and L. Zhou, Flexible and Salt Resistant Janus Absorbers by Electrospinning for Stable and Efficient Solar Desalination, *Adv. Energy Mater.*, 2018, **8**, 1702884.

25 W. Li, Z. Li, K. Bertelsmann and D. E. Fan, Portable Low-Pressure Solar Steaming-Collection Unisystem with Polypyrrole Origamis, *Adv. Mater.*, 2019, **31**, 1900720.

26 L. Wu, Z. Dong, Z. Cai, T. Ganapathy, N. X. Fang, C. Li, C. Yu, Y. Zhang and Y. Song, Highly efficient three-dimensional solar evaporator for high salinity desalination by localized crystallization, *Nat. Commun.*, 2020, **11**, 521.

27 Y. Wang, X. Wu, P. Wu, H. Yu, J. Zhao, X. Yang, Q. Li, Z. Zhang, D. Zhang, G. Owens and H. Xu, Salt isolation from waste brine enabled by interfacial solar evaporation with zero liquid discharge, *J. Mater. Chem. A*, 2022, **10**, 14470–14478.

28 L. Zhou, Y. Tan, J. Wang, W. Xu, Y. Yuan, W. Cai and S. Zhu, 3D self-assembly of aluminium nanoparticles for plasmon-enhanced solar desalination, *Nat. Photonics*, 2016, **10**, 393–398.

29 Y. Wang, L. Zhang and P. Wang, Self-Floating Carbon Nanotube Membrane on Macroporous Silica Substrate for Highly Efficient Solar-Driven Interfacial Water Evaporation, *ACS Sustain. Chem. Eng.*, 2016, **4**, 1223–1230.

30 L. Zhu, M. Gao, C. Kang, N. Peh and X. Wang, Self-Contained Monolithic Carbon Sponges for Solar-Driven Interfacial Water Evaporation Distillation and Electricity Generation, *Adv. Energy Mater.*, 2018, **8**, 1702149.

31 W. Li, Y. Shi, K. Chen, L. Zhu and S. Fan, A Comprehensive Photonic Approach for Solar Cell Cooling, *ACS Photonics*, 2017, **4**, 774–782.

32 G. Xue, K. Liu, Q. Chen, P. Yang, J. Li, T. Ding, J. Duan, B. Qi and J. Zhou, Robust and Low-Cost Flame-Treated Wood for High-Performance Solar Steam Generation, *ACS Applied Materials and Interfaces*, 2017, **9**, 15052–15057.

33 Y. Li, W. Hong, H. Li, Z. Yan, S. Wang, X. Liu, B. Li and H. Jiang, Solar absorber with tunable porosity to control the water supply velocity to accelerate water evaporation, *Desalination*, 2021, **511**, 115113.

34 Y. Sui, A flowerlike sponge coated with carbon black nanoparticles for enhanced solar vapor generation, *J. Mater. Sci.*, 2020, **55**, 298–308.

35 Z. Sun, W. Li, W. Song, L. Zhang and Z. Wang, A high-efficiency solar desalination evaporator composite of corn stalk, Mcnts and TiO2: ultra-fast capillary water moisture transportation and porous bio-tissue multi-layer filtration, *J. Mater. Chem. A*, 2020, **8**, 349–357.

36 L. Zang, L. Sun, S. Zhang, C. Finnerty, A. Kim, J. Ma and B. Mi, Nanofibrous hydrogel-reduced graphene oxide membranes for effective solar-driven interfacial evaporation and desalination, *Chem. Eng. J.*, 2021, **422**, 129998.

37 S. C. Singh, M. Elkabbash, Z. Li, X. Li, B. Regmi, M. Madsen, S. A. Jalil, Z. Zhan, J. Zhang and C. Guo, Solar-trackable super-wicking black metal panel for photothermal water sanitation, *Nat Sustainability*, 2020, **3**, 938.

38 Y. Shi, C. Zhang, R. Li, S. Zhuo, Y. Jin, L. Shi, S. Hong and J. Chang, Solar Evaporator with Controlled Salt Precipitation for Zero Liquid Discharge Desalination, *Environ. Sci. Technol.*, 2018, **52**, 11822–11830.

39 Z. Wang, J. Gao, J. Zhou, J. Gong, L. Shang, H. Ye, F. He, S. Peng, Z. Lin, Y. Li and F. Caruso, Engineering Metal – Phenolic Networks for Solar Desalination with Directional Salt Crystallization, *Adv. Mater.*, 2023, **35**, 2209015.

40 H. Li, S. Wang, X. Wang, X. Niu and Y. Li, Synchronously managed water and heat transportation for highly efficient interfacial solar desalination, *Desalination*, 2022, **538**, 115897.

41 H. Li, S. Wang, Z. Yan, X. Niu, X. Sun and W. Hong, Harvesting conductive heat loss of interfacial solar evaporator for thermoelectric power generation, *Appl. Therm. Eng.*, 2022, **208**, 118279.

42 L. Huang, H. Jiang, Y. Wang, Z. Ouyang, W. Wang and B. Yang, Enhanced water yield of solar desalination by thermal concentrated multistage distiller, *Desalination*, 2020, **477**, 114260.

43 W. Wang, Y. Shi, C. Zhang, S. Hong, Y. Jin, C. Ong, S. Zhuo and P. Wang, Simultaneous production of fresh water and electricity via multistage solar photovoltaic membrane distillation, *Nat. Commun.*, 2019, **10**, 3012.

44 Z. Xu, L. Zhang, L. Zhao, B. Li, B. Bhatia, C. Wang, K. L. Wilke, Y. Song, O. Labban, J. H. Lienhard, R. Z. Wang and E. Wang, Ultrahigh-efficiency desalination via a thermally-localized multistage solar still, *Energy Environ.*, 2020, **13**, 830–839.

45 Y. Li, X. Liu, W. Hong, X. Chen and H. Li, Formation , evolution , and enhancement mechanisms of mixed temperature gradient during interfacial solar vapor generation, *Int. J. Heat Mass Transfer*, 2023, **208**, 124082.

46 J. Yang, Y. Chen, X. Jia, Y. Li, S. Wang and H. Song, Wood-Based Solar Interface Evaporation Device with Self-Desalting and High Antibacterial Activity for Efficient Solar Steam Generation Antibacterial Activity for Efficient Solar

Steam Generation, *ACS Appl. Mater. Interfaces*, 2020, **12**, 47029–47037.

47 Z. Liu, B. Wu, B. Zhu, Z. Chen, M. Zhu and X. Liu, Continuously Producing Watersteam and Concentrated Brine from Seawater by Hanging Photothermal Fabrics under Sunlight, *Adv. Funct. Mater.*, 2019, **29**, 1905485.

48 H. Li, Z. Yan, Y. Qian, S. Wang, X. Liu and S. Yan, Hierarchically structured evaporator with integrated water supply and evaporation layers to retard salt accumulation, *Int. J. Heat Mass Transfer*, 2022, **185**, 122447.

49 Z. Wei, J. Wang, S. Guo and S. C. Tan, Towards highly salt-rejecting solar interfacial evaporation : Photothermal materials selection , structural designs , and energy management, *Nano Res. Energy*, 2022, **1**, e9120014.

50 Z. Yu, S. Li, Y. Chen, X. Zhang, J. Chu, Y. Zhang and S. ChingTan, Intensifying the co-production of vapor and salts by a one-way brine-flowing structure driven by solar irradiation or waste heat, *Desalination*, 2022, **539**, 115942.

51 Y. Wang, C. Wang, X. Song, M. Huang and S. K. Megarajan, Improved light-harvesting and thermal management for efficient solar-driven water evaporation using 3D photothermal cones, *J. Mater. Chem. A*, 2018, **6**, 9874–9881.

52 Y. Shi, R. Li, S. Hong, Y. Shi, R. Li, Y. Jin, S. Zhuo, L. Shi, J. Chang and S. Hong, A 3D Photothermal Structure toward Improved Energy Efficiency in Solar Steam Generation, *Joule*, 2018, **2**, 1171–1186.

53 M. S. Irshad, N. Arshad, X. Wang, H. R. Li, M. Q. Javed, Y. Xu, L. A. Alshahrani, T. Mei and J. Li, Intensifying Solar Interfacial Heat Accumulation for Clean Water Generation Excluding Heavy Metal Ions and Oil Emulsions, *Sol. RRL*, 2021, **5**, 2100427.

54 H. Ghasemi, G. Ni, A. M. Marconnet, J. Loomis, S. Yerci, N. Miljkovic and G. Chen, Solar steam generation by heat localization, *Nat. Commun.*, 2014, **5**, 4449.

55 X. Zhang, W. Gao, X. Su, F. Wang, B. Liu and J. Wang, Conversion of solar power to chemical energy based on carbon nanoparticle modified photo-thermoelectric generator and electrochemical water splitting system, *Nano Energy*, 2018, **48**, 481–488.

56 Y. Pang, X. Chu, L. Song, L. Jin, C. Ma, Y. Wu, L. Li, Y. Peng, X. Zheng, F. Wang, S. Wu, Z. Shen and H. Chen, Laser-engraved wood-based evaporators : A sustainable approach for solar interfacial evaporation, *Chem. Eng. J.*, 2024, **479**, 147891.

57 Y. Wu, R. Kong, C. Ma, L. Li, Y. Zheng, Y. Lu, L. Liang, Y. Pang, Q. Wu, Z. Shen and H. Chen, Simulation-guided design of bamboo leaf-derived carbon-based high-efficiency evaporator for solar-driven interface water evaporation, *Energy Environ. Mater.*, 2021, **5**, 1323–1331.

58 Z. Huang, S. Li, X. Cui, Y. Wan, Y. Xiao, S. Tian, H. Wang, X. Li, Q. Zhao and C.-S. Lee, Broadband aggregation-independent plasmonic absorber for highly efficient solar steam generation, *J. Mater. Chem. A*, 2020, **8**, 10742–10746.

59 Y. Yang, W. Que, J. Zhao, Y. Han, M. Ju and X. Yin, Membrane assembled from anti-fouling copper-zinc-tin-selenide nanocarambolas for solar-driven interfacial water evaporation, *Chem. Eng. J.*, 2019, **373**, 955–962.

60 Y. Luo, S. Fei, W. Xiu-Li and W. Yu-Zhong, Water bridge solar evaporator with salt-resistance and heat localization for efficient desalination, *J. Mater. Chem. A*, 2023, **11**, 3118–3125.

61 Q. Lu, W. Shi, H. Yang and X. Wang, Nanoconfined Water-Molecule Channels for High-Yield Solar Vapor Generation under Weaker Sunlight, *Adv. Mater.*, 2020, **32**, 2001544.

62 D. Qin, Y. Zhu, R. Yang and Z. Xiong, A salt-resistant Janus evaporator assembled from ultralong hydroxyapatite nanowires and nickel oxide for efficient and recyclable solar desalination, *Nanoscale*, 2020, **12**, 6717–6728.

63 X. Li, J. Li, X. Li, J. Li, J. Lu, N. Xu, C. Chen, X. Min, B. Zhu and H. Li, Enhancement of Interfacial Solar Vapor Generation by Environmental Energy Enhancement of Interfacial Solar Vapor Generation by Environmental Energy, *Joule*, 2018, **2**, 1331–1338.

64 Y. Kong, H. Dan, W. Kong, Y. Gao, Y. Shang, K. Ji, Q. Yue and B. Gao, Self-floating maize straw/graphene aerogel synthesis based on microbubble and ice crystal templates for efficient solar-driven interfacial water evaporation, *J. Mater. Chem. A*, 2020, **8**, 24734–24742.

65 P. Zhang, Q. Liao, H. Yao, H. Cheng, Y. Huang, C. Yang, L. Jiang and L. Qu, Three-dimensional water evaporation on a macroporous vertically aligned graphene pillar array under one sun, *J. Mater. Chem. A*, 2018, **6**, 15303–15309.

66 X. Fan, Y. Yang, X. Shi, Y. Liu, H. Li, J. Liang and Y. Chen, A MXene-Based Hierarchical Design Enabling Highly Efficient and Stable Solar-Water Desalination with Good Salt Resistance, *Adv. Funct. Mater.*, 2020, **30**, 2007110.

67 X. Han, L. V Besteiro, C. Sher, L. Koh, H. K. Lee, I. Y. Phang, G. C. Phan-quang, J. Y. Ng, H. Yi, F. Sim, C. L. Lay, A. Govorov and X. Y. Ling, Intensifying Heat Using MOF-Isolated Graphene for Solar-Driven Seawater Desalination at 98% Solar-to-Thermal Efficiency, *Adv. Funct. Mater.*, 2021, **31**, 2008904.

68 V. A. Online, D. Wu, D. Qu, W. Jiang, G. Chen, C. Zhuang, Z. Sun and L. An, Self-floating nanostructured Ni–NiOx/Ni foam for solar thermal water evaporation, *J. Mater. Chem. A*, 2019, **7**, 8485–8490.